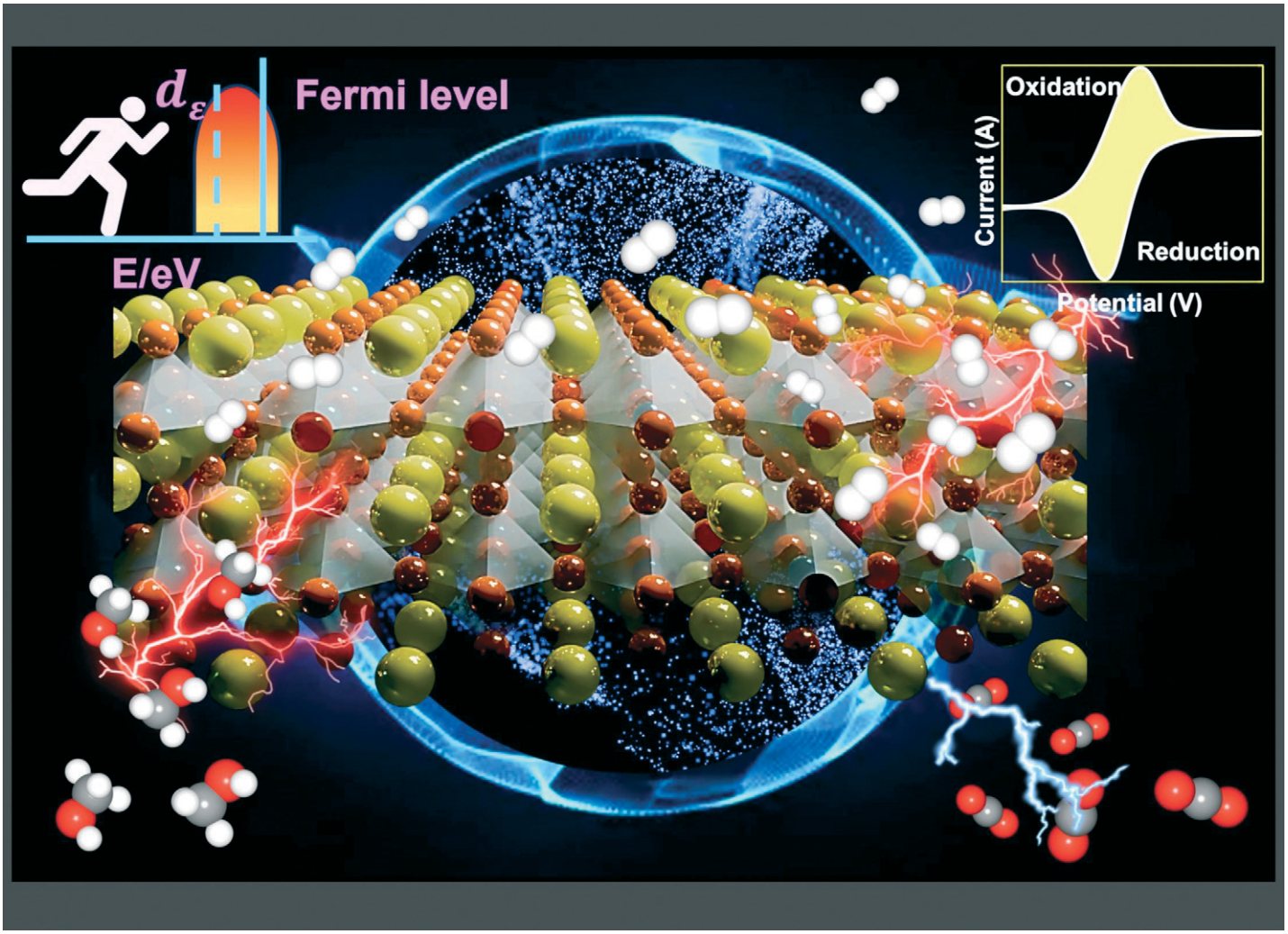

Showcasing research from Professor Ravinder Pawar's laboratory, Department of Chemistry, National Institute of Technology Warangal, Telangana, India.

Studies on the electrochemical oxidation of methanol using La_2MO_4 (M = Ni, Cu and Zn) catalysts

La_2CuO_4 (LCO) stands out by outperforming La_2NiO_4 (LNO), La_2ZnO_4 (LZO), and many reported catalysts in methanol oxidation, offering higher activity, lower onset potential, and strong CO tolerance. Its unique electronic structure ensures superior efficiency and stability, making it a promising candidate for clean energy technologies.

As featured in:

See Ravinder Pawar, Venkatesan Subramanian *et al.*, *Catal. Sci. Technol.*, 2025, **15**, 6678.

ROYAL SOCIETY OF CHEMISTRY

rsc.li/catalysis

Registered charity number: 207890

Catalysis Science & Technology

ROYAL SOCIETY OF CHEMISTRY

PAPER

View Article Online
View Journal | View Issue

Check for updates

Cite this: *Catal. Sci. Technol.*, 2025, 15, 6678

Studies on the electrochemical oxidation of methanol using La_2MO_4 (M = Ni, Cu and Zn) catalysts

Pooja,[a] Ravinder Pawar *[a] and Venkatesan Subramanian*[b]

Received 9th July 2025,
Accepted 9th September 2025

DOI: 10.1039/d5cy00827a

rsc.li/catalysis

Catalytic electrochemical oxidation of methanol is emerging as a promising alternative for clean energy production. Hence, the present investigation explores the methanol oxidation reaction (MOR) using three rare-earth metal-based oxide catalysts, La_2NiO_4 (LNO), La_2CuO_4 (LCO), and La_2ZnO_4 (LZO) —synthesized *via* a sustainable sol–gel method. Detailed characterization through various spectroscopic techniques confirms the successful synthesis of the catalysts with distinct crystalline phases and uniform microstructures. Electrochemical analysis reveals that the LCO exhibits superior MOR activity, compared to LNO and LZO catalysts, which is further supported by density functional theory (DFT) calculations. LCO exhibits a lower Tafel slope (42 mV dec^{-1}) than LNO (220 mV dec^{-1}) and LZO (233 mV dec^{-1}). The most favourable pathway of oxidation of methanol using the LCO catalyst primarily involves C–H bond dissociation. The anti-poisoning effect of the LCO catalyst, confirmed by CO stripping analysis, ^{13}C NMR, ^{1}H NMR, and FTIR spectroscopy, demonstrates its strong resistance to CO poisoning and high catalytic efficiency, highlighting its potential as a promising catalyst for renewable energy applications.

Introduction

The methanol oxidation reaction (MOR) is a benchmark electrochemical process for studying the interaction of small organic molecules with metal-based electrocatalysts, offering insight into reaction pathways relevant to energy conversion.[1–4] The process yields valuable intermediates like formic acid, formaldehyde, and CO_2, indicating its mechanistic complexity. Among electrocatalysts, platinum (Pt) has been widely studied due to its superior activity and selectivity.[5–16] However, Pt-based systems suffer from severe drawbacks, including susceptibility to CO poisoning due to strong CO adsorption, high cost, limited abundance, and poor long-term stability.[5–16] These challenges hinder their practical deployment in direct methanol fuel cells (DMFCs).[3,17,18]

Recent efforts have focused on rare-earth-based materials, particularly those combining lanthanides with late 3d transition metals (TMs) such as Mn, Fe, Co, Ni, Cu, or Zn.[19–27] These materials offer promising features, including tunable redox chemistry, structural flexibility, high oxygen mobility, and enhanced corrosion resistance.[19–27] Despite their chemical inertness stemming from 4f orbitals shielded by 5s and 5p orbitals, rare earth elements play a pivotal role in electrocatalysis. Lanthanum-based materials, in particular, stand out for their versatility, finding use in organic catalysis, electrochemical electrodes, and propellant enhancement owing to their variable occupation in f-orbital and its interaction.[28–36] Among them, lanthanum-based oxides have attracted increasing attention due to their unique A_2BO_4-type structures and potential for oxygen intercalation, which can significantly enhance electronic conductivity and catalytic behavior.[37,38] For instance, La_2CuO_4 (LCO) has shown superconductivity and fast oxygen transport properties, while La_2NiO_4 (LNO) exhibits superior mixed ionic–electronic conductivity. La_2ZnO_4 (LZO), though less explored, has shown promise as a redox-active material.[39–45]

Lanthanum-based materials have been widely studied across various catalytic and electronic applications. However, studies on comprehensive investigations of their use as electrocatalysts for methanol oxidation and reaction mechanism pathways remain limited.[25,46–50] Recent studies have shown that MOR activity is highly influenced by the type of the transition metal atom within the oxide framework. Substituting different 3d metals not only alters the electronic structure but also impacts surface adsorption, reaction kinetics, and overall efficiency.[25,46–50] Despite progress, the precise role of the transition metal in governing catalytic

[a] *Laboratory of Advanced Computation and Theory for Materials and Chemistry (LACTMC), Department of Chemistry, National Institute of Technology Warangal (NITW), Warangal, Telangana-506004, India. E-mail: ravinder_pawar@nitw.ac.in*
[b] *Department of Chemistry, Indian Institute of Technology Madras, Chennai, 600036 India. E-mail: subuchem@hotmail.com*

behavior, as well as the contribution of the rare-earth element (La^{3+}), remains underexplored. Additionally, the oxidation states of metal ions are critical in determining catalytic activity. Deviations from ideal stoichiometry due to oxygen vacancies or excess can significantly affect charge transport properties and surface reactivity.[51] This redox flexibility influences intermediate binding strengths and, consequently, both activity and selectivity in the MOR. A major challenge in the MOR is CO poisoning, where strongly adsorbed CO intermediates deactivate the active sites and limit long-term stability. Furthermore, while La-based mixed metal oxide has been hypothesized to show enhanced CO tolerance due to its redox flexibility and surface oxygen dynamics, direct validation in the context of MOR is still sparse.

To address these gaps, this study systematically investigates La_2MO_4 (M = Ni, Cu, Zn) catalysts for the MOR using a combined experimental and theoretical approach. The catalysts were synthesized *via* a facile sol–gel method and comprehensively characterized by powder X-ray diffraction (PXRD), field emission scanning electron microscopy (FESEM), energy-dispersive X-ray spectroscopy (EDS), X-ray photoelectron spectroscopy (XPS), and high-resolution transmission electron microscopy (HRTEM). Electrochemical performance was assessed *via* cyclic voltammetry (CV), with LCO demonstrating superior MOR activity compared to LNO and LZO. Among the series, LCO exhibited the most promising performance, with a lower onset potential (~1.15 V *vs.* RHE) and reduced Tafel slope compared to LNO and LZO. Density functional theory (DFT) calculations further support the experimental findings by revealing favorable methanol adsorption energies, reaction intermediates, and pathways on LCO surfaces. The energy and *k*-point convergence test is provided in SI section S1B and Fig. S1. This suggests that the superior activity of LCO arises from its optimal electronic structure and higher density of active sites. Overall, this integrated study deepens the understanding of how transition metal substitution and rare-earth metal coordination govern MOR activity and stability in the considered electrocatalysts.

Results and discussion

Characterization

The LNO, LCO, and LZO catalysts were synthesized using a straightforward and sustainable sol–gel approach (Fig. 1), using standard reagents including lanthanum(III) nitrate hexahydrate ($La(NO_3)_3{\cdot}6H_2O$, 99%), copper(II) nitrate trihydrate ($Cu(NO_3)_2{\cdot}3H_2O$, 99%), nickel(II) nitrate hexahydrate ($Ni(NO_3)_2{\cdot}6H_2O$, 99%), zinc nitrate hexahydrate ($Zn(NO_3)_2{\cdot}6H_2O$, 99%), citric acid (CA) ($HOC(COOH)(CH_2COOH)_2$, 99%), and ammonia (NH_3) solution, purchased from the Sigma Aldrich. Detailed computational methodologies, synthesis protocols, and convergence details are provided in SI section S1 and Fig. 1. The sol–gel method was chosen for its simplicity, reproducibility, and ability to form a porous structure. The morphology and crystalline phases of the catalysts were examined using various spectroscopic techniques. The pictorial representation of the crystal structure for LNO, LCO, and LZO catalysts is provided in Fig. 2a–c.

The FESEM analysis provides detailed insights into the topology of the synthesized catalysts, elemental distribution, and element mapping of the crystal surfaces. The FESEM topography clearly shows that the LNO, LCO, and LZO catalysts exhibit a dense microstructure, characterized by well-grown grains approximately 100 nm in size (see Fig. 2d–f). Following the analysis of the FESEM results, we conducted an elemental mapping at 1 μm of the considered catalysts, which confirmed the presence of all anticipated elements in the samples. The EDS results display the characteristic peaks and atomic ratios associated with the elements, as shown in Fig. 2d–f, and the SI (section S2 and Fig. S2), which further confirm the formation of synthesized materials.

PXRD analysis was conducted to determine the crystalline structure and phase purity of the synthesized LNO, LCO, and LZO catalysts. Rietveld refinement was performed by systematically adjusting parameters using GSAS II software.[52] The PXRD pattern of LNO, shown in Fig. 2g, displays well-defined peaks at 2θ = 30.9°, 40.3°, 44.3°, 51.6°, 58.3°, 67.4°, and 78.8°, corresponding to the (111), (120), (121), (202),

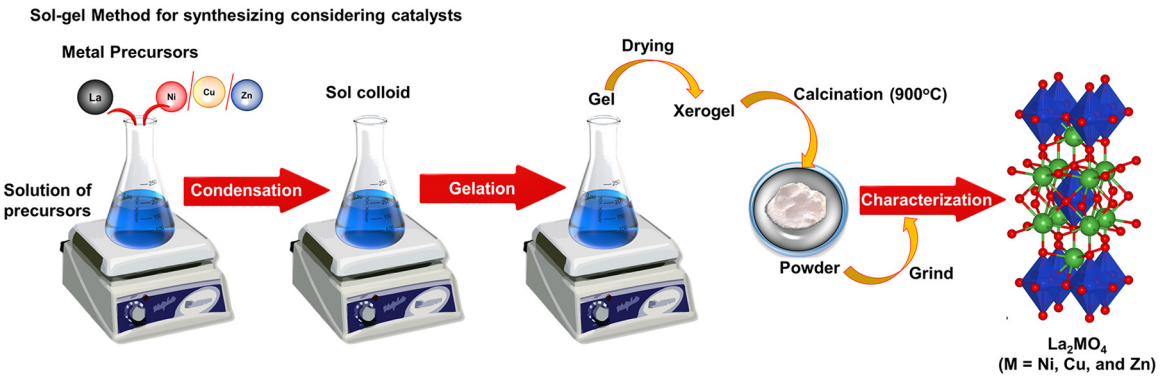

Fig. 1 Schematic representation of the La_2MO_4 synthesis process. Color code: red: oxygen, green: lanthanum, and blue polyhedral represents the position of metal atom M.

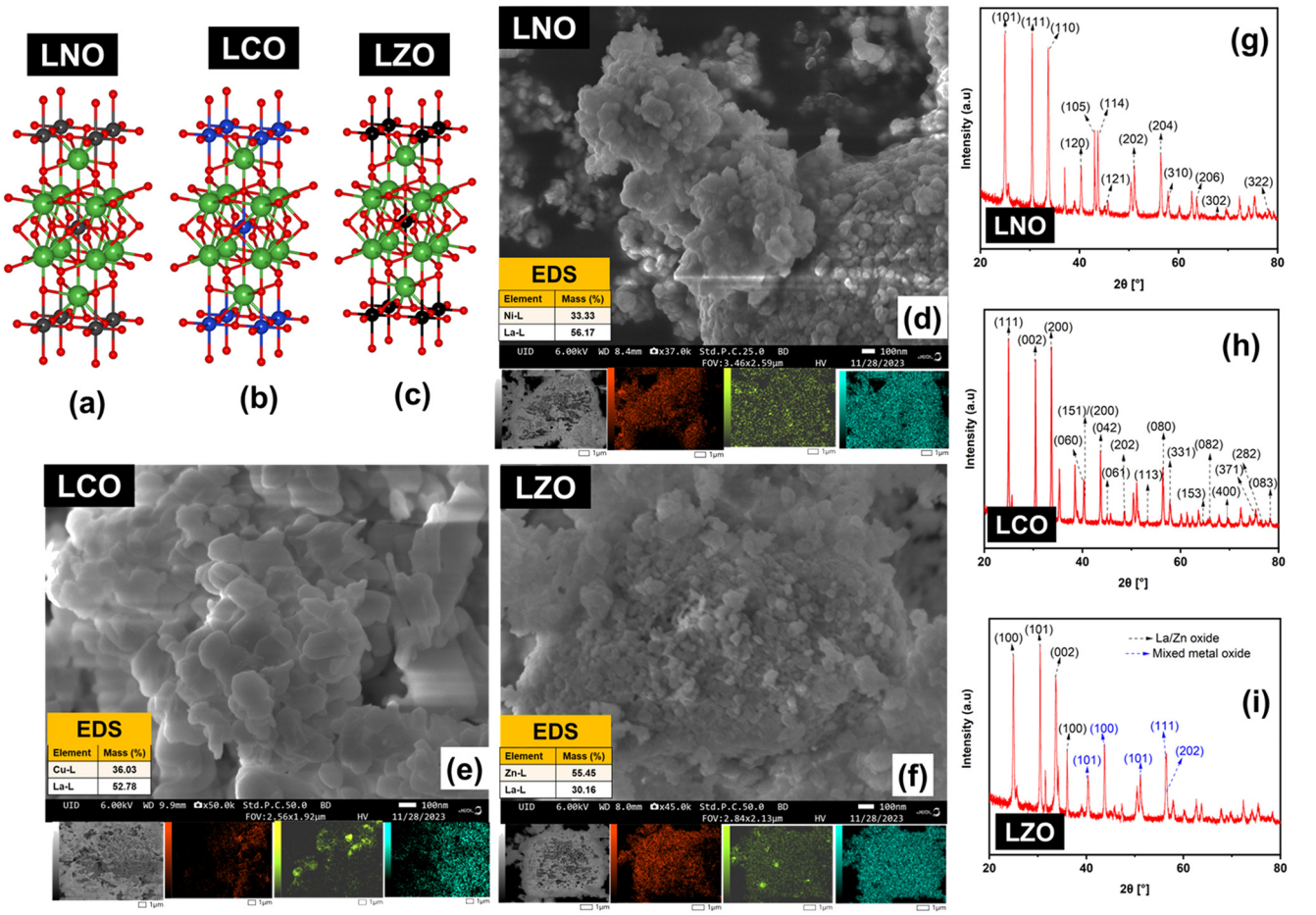

Fig. 2 Optimized supercell cell of (a) LNO, (b) LCO, and (c) LZO; FESEM image of (d) LNO, (e) LCO, and (f) LZO; and PXRD plot of (g) LNO, (h) LCO, and (i) LZO. Color code: red: oxygen, green: lanthanum, grey: nickel, blue: copper, and black: zinc.

(310), (302), and (322) planes, respectively, as referenced in PDF#34-0984. Additional reflections are observed at 24.0° (101), 32.7° (110), 42.7° (105), 43.7° (114), 56.3° (204), and 63.6° (206), aligning well with the tetragonal phase of La_2NiO_4 (space group *I*4/*mmm*), as referenced in PDF#80-1346. These results confirm the successful synthesis of a single-phase, highly crystalline LNO material, in agreement with previous literature reports.[53–58]

For LCO, the PXRD profile (Fig. 2h) exhibits intense diffraction peaks at 2θ = 24.3°, 27.1°, 31.1°, 33.1°, 33.4°, 41.2°, 41.7°, 43.5°, 47.8°, 54.0°, 54.4°, 55.8°, 58.0°, 64.9°, 65.1°, 69.6°, 70.0°, 75.3°, 76.5°, and 78.5° corresponding crystallographic planes (111), (004), (113), (020), (200), (006), (115), (204), (220), (206), (117), (224), (133), (226), (135), (040), (400), (331), (228), and (333). The diffraction pattern corresponds closely with the standard orthorhombic phase of La_2CuO_4 (PDF#82-2142, space group *Bmab*), confirming the formation of a phase-pure LCO perovskite upon calcination at 900 °C for 2 h. A few minor peaks at 2θ = 35.9°, 38.9°, and 49.1° were also detected, indicative of a trace CuO phase (PDF#80-1917), suggesting slight phase segregation during synthesis. Nonetheless, the dominant phase remains orthorhombic La_2CuO_4 with high crystallinity and structural integrity, consistent with previous findings.[59–63]

The PXRD pattern for the LZO catalyst (Fig. 2i) reveals diffraction peaks attributable to a mixed oxide system of La and Zn. Notable peaks at 2θ = 31.0° (101) and 36.0° (100) are consistent with overlapping reflections from both La- and Zn-based oxides. Additional diffraction features at 40.0° (101), 42.3° (100), 51.0° (101), and 55.0° (111) further confirm the formation of a homogeneous La–Zn oxide composite.[64–66]

Notably, no diffraction peaks corresponding to La_2O_3, such as (100) at 15.7° and (211) at 48.8°, were observed,[67] affirming the absence of unreacted lanthanum oxide in LCO, LNO and LZO catalysts as shown in SI section S3 and Fig. S3a.

The XPS was employed to investigate the surface chemical composition and electronic structure of the LNO, LCO, and LZO catalysts, offering valuable insights into their surface properties. The surface composition, fitting results, and binding energies of each element present in LNO, LCO, and LZO catalysts are presented in the SI (section S3 and Tables S1a–d). Fig. 3a(i–iii) shows the O 1s, Ni 2p and La 3d XPS spectra for the LNO catalyst. The O 1s spectrum was deconvoluted into distinct peaks, with the peak at 530.6 eV

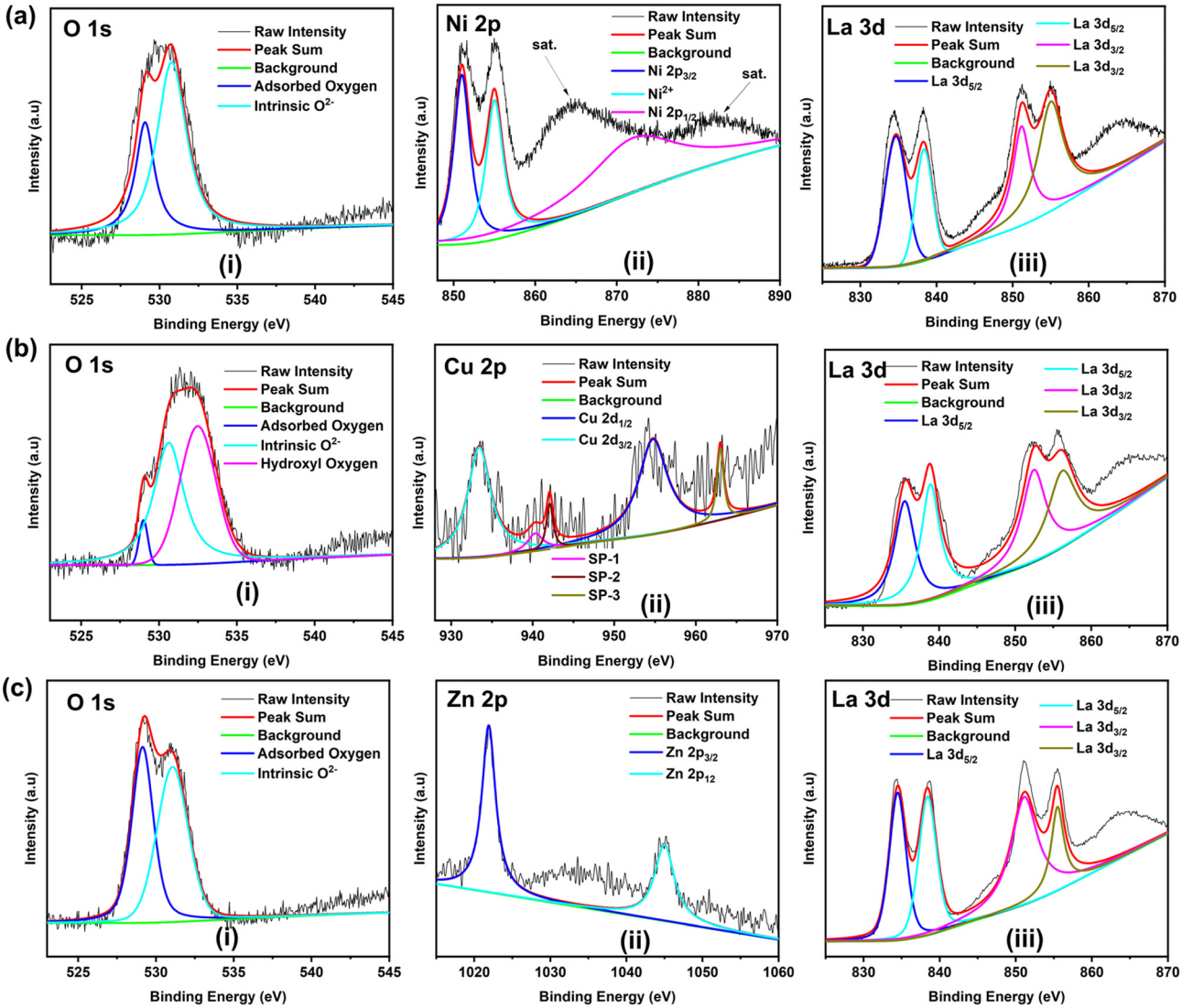

Fig. 3 XPS analysis of (a) LNO, (b) LCO, and (c) LZO catalysts (where (i) O 1s, (ii) transition metal 2p (Ni, Cu, Zn), and (iii) La 3d core levels, respectively).

indicating oxygen in the Ni–O bond. The La–O bond is ionic, while the Ni–O bond is covalent. The high-resolution Ni 2p spectrum of the LNO sample displays prominent peaks of Ni $2p_{3/2}$ and Ni $2p_{1/2}$. Additionally, the high-resolution La 3d spectrum reveals four distinct peaks at 834.65 eV, 838.35 eV, 851.15 eV, and 855.01 eV, corresponding to La $3d_{5/2}$ and La $3d_{3/2}$, indicating the presence of La^{3+}. However, due to the presence of significant overlapping between the Ni $2p_{3/2}$ and La $3d_{3/2}$ satellite peaks of Ni 2p and La 3d, the core-level spectra of La 3d and Ni 2p were not analyzed further.

Similarly, Fig. 3b(i) shows that the peak around 529.00 eV in the O 1s spectra corresponds to oxygen in the La–O bond for the LCO catalyst. The La 3d spectra exhibit two doublets due to spin–orbital splitting, with main peaks at 835.48 eV and 852.44 eV, and satellite peaks at 838.48 eV and 856.17 eV, assigned to La $3d_{5/2}$ and $3d_{3/2}$, respectively (Fig. 3b(iii)). The Cu 2p spectrum (Fig. 3b(ii)) reveals two components at binding energies of 933.42 eV (Cu $2p_{3/2}$) and 954.74 eV (Cu $2p_{1/2}$), with a peak separation of 20.9 eV, confirming the presence of Cu^{2+}. The peaks at 940.28 eV, 942.07 eV, and 963.00 eV are attributed to the oscillation of the Cu^{2+} structure consisting of different kinds of spin–orbit lines, called SP-1, SP-2, and SP-3, respectively. The La 3d and Cu 2p spectra confirm the presence of only La^{3+} and Cu^{2+} on the LCO surface. XPS analysis for the LCO catalyst is also provided in the SI (section S3 and Fig. S3b).

The XPS spectrum for the LZO catalyst is provided in Fig. 3c(i–iii). In the O 1s spectrum, the peak at 529.0 eV indicates oxygen in the Zn–O bond, while the peak at 531.06 eV corresponds to oxygen in the La–O bond. The peaks at 834.47 eV and 855.47 eV are assigned to La $3d_{5/2}$ and La $3d_{3/2}$, respectively, characteristic of La^{3+}. The Zn 2p spectrum shows peaks at 1021.89 eV and 1045.00 eV, corresponding to Zn^{2+} (Zn $2p_{3/2}$ and Zn $2p_{1/2}$). The La 3d peaks for LNO, LCO, and LZO are observed between 830–851 eV and 837–855 eV for $3d_{5/2}$ and $3d_{3/2}$, respectively, indicating La^{3+}. Additionally,

lower binding energy peaks (527–530 eV) in the O 1s spectrum correspond to stoichiometric O^{2-}, while lattice oxygen is indicated by peaks at ~528.5 and ~530.3 eV. The binding energy at ~531.1 eV suggests the presence adsorbed oxygen.

The FTIR analysis of the LMO catalyst revealed the formation of La_2MO_4 which is also supported by PXRD and XPS analysis. The detailed discussion of the various FTIR stretching frequencies of the metal oxide is provided in the SI (section S4 and Fig. S4). The FTIR spectra reveal peaks at higher wavenumbers that are related to hydrogen and oxygen bonds. The peak observed in the range of 500–600 cm^{-1} typically corresponds to metal–oxygen (M–O) stretching vibrations, which are characteristic of the A_2BO_4-type structure.[65,68–72] The peak at 653–679 cm^{-1} is attributed to the La–O stretching vibration along the *c*-axis, while the 503–523 cm^{-1} band is assigned to the Ni–O stretching vibration. The chemical structure of the LCO binary oxide was further examined using FTIR spectroscopy.[68,71,72] The low-intensity bands observed at 502 and 1065 cm^{-1}, as well as at 591 and 1108 cm^{-1}, are associated with Cu–O and La–O stretching modes, respectively, which are characteristic of the orthorhombic LCO phase. Additionally, the presence of bands at 596 and 1187 cm^{-1}, corresponding to Cu–O stretching modes, in all the samples indicates the formation of Cu–O as a secondary phase. This is likely due to the 1 : 1 precursor ratio used, resulting in the formation of an A_2BO_4-type structure.[69,70] Similarly, the FTIR spectrum of the LZO catalyst exhibits characteristic peaks at 529.4 and 1479 cm^{-1}, which are attributed to Zn–O stretching vibrations. A distinct peak at 609 cm^{-1} further supports the presence of intrinsic Zn–O stretching. Moreover, the broad peak observed in the range of 450–550 cm^{-1} is often associated with bridging vibrations or bending modes involving both La and Zn

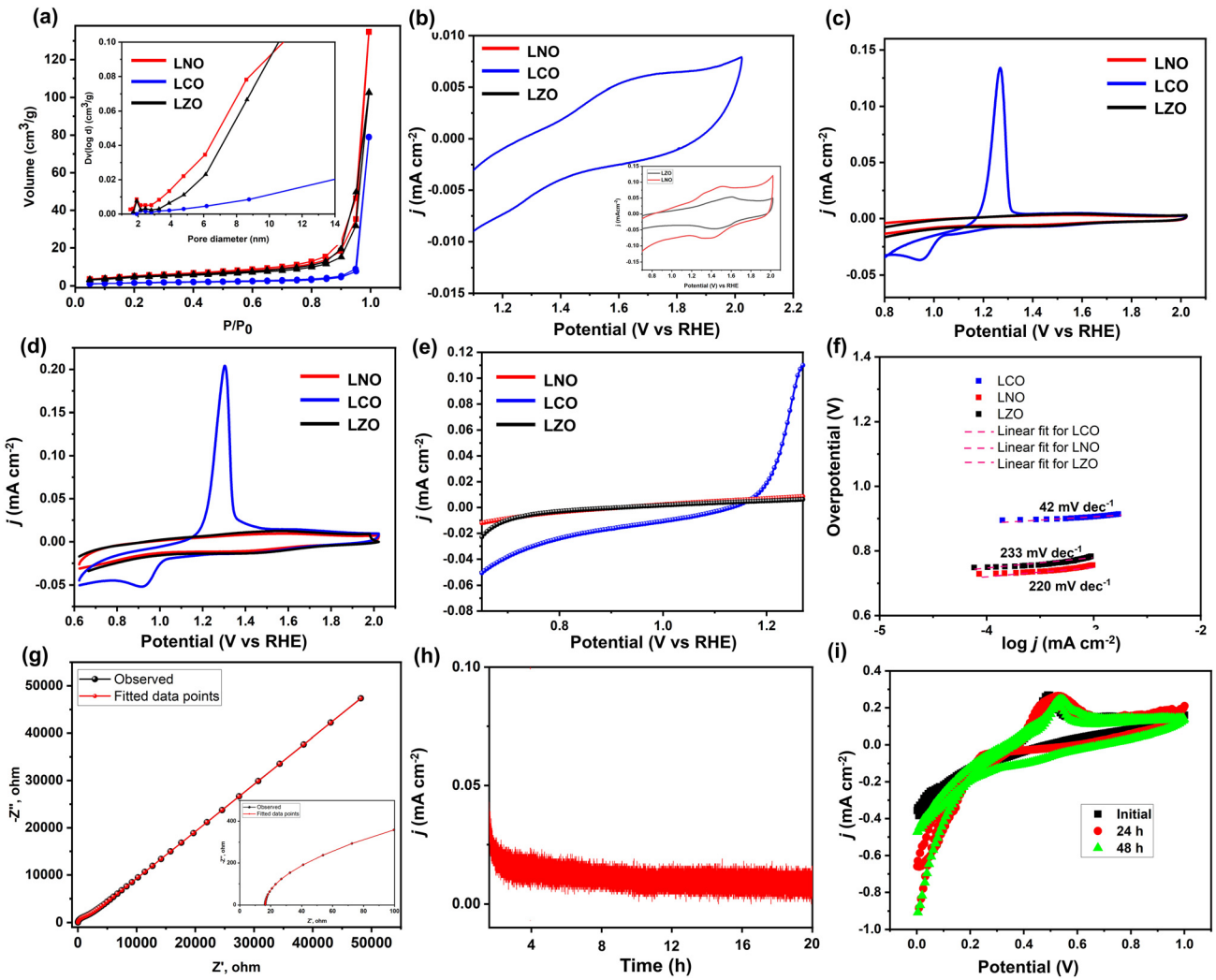

Fig. 4 (a) N_2 adsorption and desorption isotherms, along with the (insets) pore size distribution graph, (b) CVs in 0.5 M H_2SO_4 at 100 mV s^{-1} *vs.* RHE, CVs for the MOR in (c) 0.5 M H_2SO_4 + 0.5 M CH_3OH solution at a scan rate of 50 mV s^{-1} *versus* the RHE, and (d) 0.5 M H_2SO_4 + 0.5 M CH_3OH solution at a scan rate of 20 mV s^{-1} *versus* the RHE, (e) LSV curve at 0.5 M H_2SO_4 + 0.5 M CH_3OH solution at a scan rate of 50 mV s^{-1} *versus* the RHE, (f) Tafel plot, (g) Nyquist plot, (h) chronoamperometry (*I*–*t*) curve, and (i) CVs in 0.5 M H_2SO_4 + 0.5 M CH_3OH solution at a scan rate of 100 mV s^{-1}.

atoms.[73] The FTIR analysis also revealed a prominent absorption band at 806 cm^{-1}, which is attributed to the M–O–M (metal–oxygen–metal) stretching vibration, suggesting the formation of structural linkages between La and the transition metal through bridging oxygen atoms.

Catalysis

The physical properties of the catalysts were measured using N_2 adsorption, including N_2 adsorption–desorption isotherms and pore size distribution maps, as shown in Fig. 4a. Additionally, the BET surface area, pore size, and pore volume were also scrutinized. The adsorption–desorption curves of the catalysts display type IV isotherms with hysteresis loops, indicating that the considered catalysts are mesoporous. The pore size distribution diagram reveals that all materials exhibited notable advantages within the 2–10 nm range, corroborating their mesoporous nature (mesoporous materials have pore sizes ranging from 2 to 50 nm). The BET specific surface areas of the LNO, LCO, and LZO catalysts were approximately 16.44, 5.40, and 18.45 $m^2\ g^{-1}$, respectively. Fig. 4a(insets) shows the pore size distributions of the catalysts, calculated using the Barrett–Joyner–Halenda (BJH) model from desorption data. The total pore volumes for the LNO, LCO, and LZO catalysts are approximately 0.158, 0.122, and 0.208 $cm^3\ g^{-1}$, respectively.

The interaction of catalysts with methanol, including their adsorption and desorption behavior, varies significantly across materials due to differences in composition, morphology, porosity, and surface area. These factors critically influence the availability of methanol at catalytic sites, thereby affecting the observed current density. To investigate this, various electrochemical measurements were performed, as illustrated in Fig. 4b–h. The performance of the synthesized nanocatalysts for the MOR was evaluated in acidic solutions using cyclic voltammetry. Fig. 4b presents the CV curves of LMO oxides recorded in 0.5 M H_2SO_4 at a scan rate of 100 mV s^{-1} in the absence of methanol. Notably, no significant MOR oxidation peaks were observed for the considered catalysts. Consequently, the MOR activity was further analyzed in an electrolyte solution of 0.5 M H_2SO_4 + 0.5 M CH_3OH at various scan rates, as depicted in Fig. 4c and d. A substantial shift in the CV curve was observed for LCO, with a distinct oxidation peak at approximately 1.27 V *versus* the RHE and a current density of 0.13 mA cm^{-2} at a scan rate of 50 mV s^{-1}, signifying pronounced MOR activity. In contrast, no visible MOR oxidation peaks were detected for LNO and LZO catalysts. Therefore, further detailed analysis of methanol electrooxidation focuses exclusively on the LCO catalyst. The electrochemically active surface areas (ECSAs) of the electrocatalysts were determined to be 0.98 $cm^2\ g^{-1}$ for LNO, 1.67 $cm^2\ g^{-1}$ for LCO, and 0.56 $cm^2\ g^{-1}$ for LZO, respectively. The detailed ECSA calculation for the considered catalyst is provided in the SI (section S5 and Fig. S5).

The LCO catalyst demonstrated a distinct anodic peak in both the forward (I_f) and reverse (I_b) scans. The peak observed during the forward scan corresponds to methanol oxidation catalyzed by the LCO coated electrode, whereas the hysteresis in the reverse scan is attributed to the oxidation of intermediate species generated during the forward scan. Fig. S6 and S7 (SI) confirm a linear relationship between peak current and scan rate, indicative of diffusion-controlled electrochemical behavior.

The electrocatalytic activity of the synthesized materials toward the MOR was investigated using linear sweep voltammetry (LSV) in an electrolyte comprising 0.5 M H_2SO_4 and 0.5 M CH_3OH, scanned at 50 mV s^{-1} over a consistent potential window. In the presence of methanol, a marked increase in current density was observed, indicating significant catalytic activity, although no distinct redox peaks corresponding to the metal ions were evident. This behavior suggests that the materials effectively facilitate methanol oxidation without involving direct redox transitions of the metal centers. Among the tested catalysts, LCO exhibited a clear onset potential of approximately 1.15 V *vs.* RHE (Fig. 4e), followed by a steep rise in current density, confirming its superior electrocatalytic performance. In contrast, the LNO and LZO catalysts did not display any discernible oxidation peaks or appreciable current response under the same conditions, indicating their poor activity toward the MOR. The absence of methanol oxidation features in LNO and LZO further highlights the enhanced performance of LCO. This superior activity can be attributed to the high surface area and feather-like porous architecture of LCO, which not only promote efficient diffusion of methanol molecules to the active sites but also facilitate rapid desorption of oxidation intermediates, thereby accelerating the overall reaction kinetics.

The Tafel slope, derived from LSV curves using the Tafel equation (Fig. 4f), was significantly lower for LCO during methanol oxidation compared to LNO and LZO. A lower Tafel slope corresponds to a higher exchange current density at the catalyst–electrolyte interface, indicating faster reaction kinetics and enhanced electrocatalytic efficiency. This observation highlights the superior MOR activity of LCO and reflects its higher ECSA relative to LNO and LZO. These results strongly support the selection of LCO for further investigation.

To gain deeper insights into the charge transfer characteristics, electrochemical impedance spectroscopy (EIS) was performed for the LCO catalyst, as shown in Fig. 4g. The Nyquist plot reveals a well-defined semicircular arc in the low-frequency region, characteristic of the charge transfer process occurring at the electrode–electrolyte interface. LCO exhibited a remarkably low charge transfer resistance (R_{ct}) of 0.02 Ω, confirming its superior electrochemical conductivity and fast interfacial electron transfer. In comparison, the R_{ct} values for LNO and LZO were substantially higher (details and equivalent circuit models are presented in SI section S5 and Fig. S5), indicating their sluggish reaction kinetics. The

EIS results further reinforce the conclusion that LCO possesses favorable electronic and interfacial properties, making it a highly promising candidate for efficient and rapid methanol electro-oxidation in energy conversion applications.

Chronoamperometric (*I–t*) measurements for the LCO catalyst revealed excellent electrochemical stability, maintaining a steady current density for approximately 12 hours at 1.0 V *vs.* RHE, with a marginal retention of activity extending up to 20 hours (Fig. 4h). During methanol oxidation, intermediate species such as CO and CH_xO can adsorb onto the catalyst surface, leading to poisoning and a gradual decline in current density over time. Therefore, poison tolerance, defined as the catalyst's ability to resist deactivation by these adsorbed intermediates, is a critical parameter for evaluating the long-term performance of electrocatalysts in practical applications. To rigorously assess the durability of the electrode materials, CV was performed at a scan rate of 100 mV s^{-1} for 100 consecutive cycles (SI section S5 and Fig. S6a–c). The LCO catalyst exhibited minimal degradation, indicating excellent structural and electrochemical stability under repeated cycling. Extended stability was further validated by subjecting the catalyst to 1300 CV cycles at the same scan rate (SI section S5 and Fig. S6d). A gradual decrease in current density was observed with increasing cycle number, which can be attributed to transient surface passivation caused by the accumulation of reaction intermediates that block active catalytic sites.

To determine the reversibility of this performance loss, the same LCO electrode was reused after resting for 24 and 48 hours in freshly prepared electrolyte (0.5 M H_2SO_4 + 0.5 M CH_3OH), as shown in Fig. 4i. The resulting CV curves displayed only minor variations in current density, with negligible shift in the anodic peak potential or intensity relative to the initial cycle. This recovery strongly suggests that the observed degradation was not due to structural decomposition of the catalyst but was instead a result of electrolyte exhaustion and surface fouling by reversible adsorbates. Upon renewal of the electrolyte, these intermediates were effectively oxidized, thereby reactivating the catalyst surface and restoring its performance.

Additionally, CV analysis of LCO was conducted across a range of scan rates (20–500 mV s^{-1}) in the same methanol-containing electrolyte to evaluate the electrochemical behavior and diffusion characteristics (SI section S5 and Fig. S7). These findings collectively reinforce the high durability, poisoning tolerance, and practical viability of LCO as a robust electrocatalyst for methanol electro-oxidation applications.

CO-poisoning analysis

The electrocatalyst (with metal constitution) deactivation in electrochemical oxidation of methanol is primarily attributed to the strong adsorption of active intermediate CO on the catalytic sites. Hence, the stability analysis of catalyst received prominent attention. In the present investigation, to probe the anti-poisoning mechanism of the LCO catalyst, CO stripping analysis was conducted. The results, presented in the SI (section S6 and Fig. S8), demonstrate the anti-CO poisoning capability of LCO. The first two cycles of the CO-stripping analysis exhibit a significant reduction in the CO oxidation peak. However, by the third and fourth cycles, complete oxidation of the CO molecules in the solution is observed. The lower oxidation onset potential (0.07 V) indicates superior anti-poisoning ability. The absence of an oxidation peak confirms that CO has been fully oxidized, leaving no residual CO molecules adsorbed on the LCO surface. Experimental techniques, including ^{13}C NMR, ^{1}H-NMR, and FTIR spectroscopy, further confirm the absence of CO peaks after electro-catalysis, providing strong evidence that CO desorbs from the LCO catalyst surface (SI sections S7–S9 and Fig. S9–S11). This desorption significantly mitigates CO poisoning, as supported by the data presented in SI sections S6–S9. Additionally, ^{13}C and ^{1}H-NMR analysis of the liquid electrolyte after methanol oxidation confirmed the complete conversion of CH_3OH to CO_2, with no by-products detected. The absence of IR peaks for CO after electro-catalysis further supports that the CO does not remain adsorbed on the LCO surface, underscoring its effective anti-poisoning behavior. Overall, the electrocatalytic studies identified LCO as the most active catalyst compared to LNO and LZO, which is likely due to its favorable electronic properties. These findings highlight the potential of LCO as an efficient and durable catalyst for methanol oxidation in acidic media. Thus, DFT calculations were performed to achieve an in-depth understanding of the structure, stability, and properties of LNO, LCO, and LZO catalysts.

Density functional theory analysis

To better understand the atomic arrangements, the crystal structures of LNO, LCO, and LZO were optimized using the generalized gradient approximation (GGA) with the Perdew–Burke–Ernzerhof (PBE) functional, as implemented in the Vienna *ab initio* simulation package (VASP).[74–78] Spin polarization effects were considered during the optimization process. A minor variation was observed in the La–O bond lengths: 2.65 Å in LNO, 2.64 Å in LCO, and 2.63 Å in LZO. The M–O bonds (M = Ni, Cu, Zn) remained nearly constant at ~1.90 Å across all systems. The La–M distance was 3.26 Å in LNO and LCO, with a slight reduction to 3.25 Å in LZO.

To explore the origins of the electrocatalytic behavior of the LMO catalysts, their electronic properties were investigated. Fig. 5 presents the calculated total density of states (TDOS), projected density of states (PDOS), and Tauc plot. Detailed spin-polarized band structure calculations are available in the SI (section S10 and Fig. S12), and electron localization function (ELF) analysis is provided in the SI (section S11 and Fig. S13).

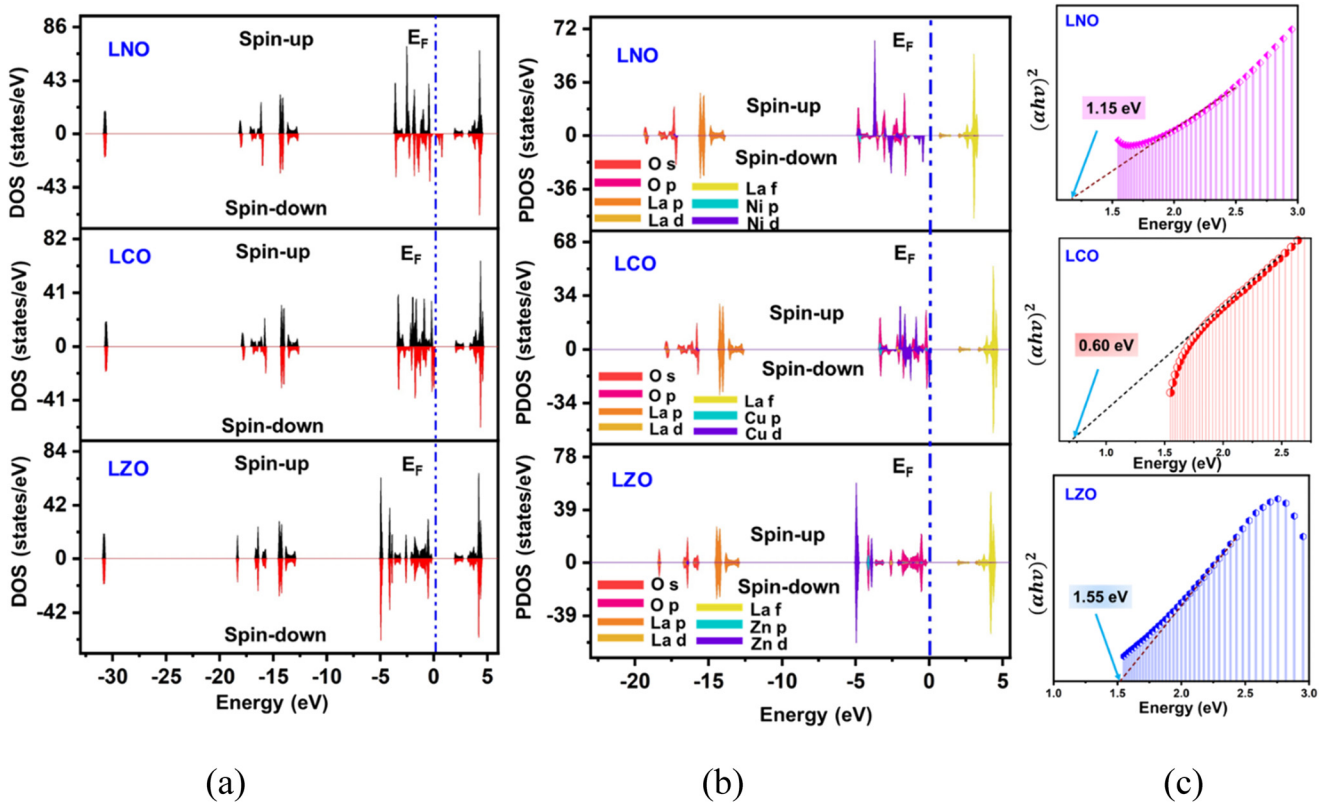

Fig. 5 Calculated (a) total density of state, (b) projected density of state, and (c) Tauc plot for the considered catalysts.

Analysis of the PDOS (Fig. 5) reveals that in the LNO catalyst, the interaction between O 2p and Ni 3d states is primarily localized between −0.69 and −4.83 eV. For the LCO and LZO catalysts, the interaction between O 2p and Cu/Zn 3d states is mainly localized between −0.08 to −3.31 and −0.31 to −5.06 eV, respectively. Notably, strong interactions between Cu 3d states and O 2p states are observed from −0.08 to −1.30 eV. In contrast, the interactions between Ni and Zn 3d states and O 2p states are minimal at the Fermi level (E_F) for LNO and LZO.

In the LMO catalysts, where M represents Ni, Cu, or Zn, the incorporation of different metal ions leads to the splitting of the d orbitals into t_{2g} and e_g states. This splitting results in a valence band below the Fermi level, comprising the occupied M t_{2g} and e_g orbitals, as well as O 2p orbitals, while the unoccupied e_g orbitals above the Fermi level contribute to the conduction band. The calculated band gaps at the Γ point are 0.30 eV for LNO and 2.09 eV for LZO, whereas the experimental values are 1.15 and 1.55 eV, respectively. The DOS and PDOS analysis for LCO predicts the electron density at the Fermi level; however, the Tauc plot yields a lower band gap value of 0.60 eV. The PBE method tends to overestimate the band gap, resulting in a small discrepancy between theoretical and experimental values for LNO, LCO, and LZO.

The high electrocatalytic performance of LCO in the MOR can be attributed to several factors. One critical aspect is its distinct morphology, which enhances MOR performance by facilitating ion and mass transport both within the catalyst structure and at the electrode–electrolyte interface. Another contributing reason is its exceptional electronic conductivity, which arises from the synergistic interaction between Cu and O atoms, resulting in reduced charge transfer resistance. The narrow band gap of LCO imparts metallic properties, facilitating the movement of electrons from the valence band to the conduction band. Significant overlap between the t_{2g} and e_g orbitals of Cu^{2+} and the O 2p orbitals within the valence band is observed, likely due to the proximity of Cu^{2+} (3d states with e_g symmetry) to the equatorial oxygen atoms.[79–84] This enhances the covalency between Cu 3d and O 2p orbitals, leading to band hybridization and potential pinning of the Fermi level at the top of the O 2p band.[79–84] This pinning significantly affects the stability of lattice oxygen in LCO oxides, making them more prone to oxidation.[79–84] Furthermore, the DOS and PDOS analysis of the LCO catalyst reveals that the bonding and antibonding orbitals near the Fermi level are primarily concentrated on the surface Cu and O sites, indicating high electroactivity. A gap state was also identified near the La and O sites. The La orbitals contribute mainly to the conduction band, and the combined contributions of La, Cu, and O to the gap state help lower the electron transfer barrier. The observation of electron density at the Fermi level further supports the efficient electron transfer during the reaction. Furthermore, the enhanced covalency in LCO contributes to its superior catalytic activity compared to LNO and LZO, as supported by the CV analysis. Overall, the metallic characteristics of LCO

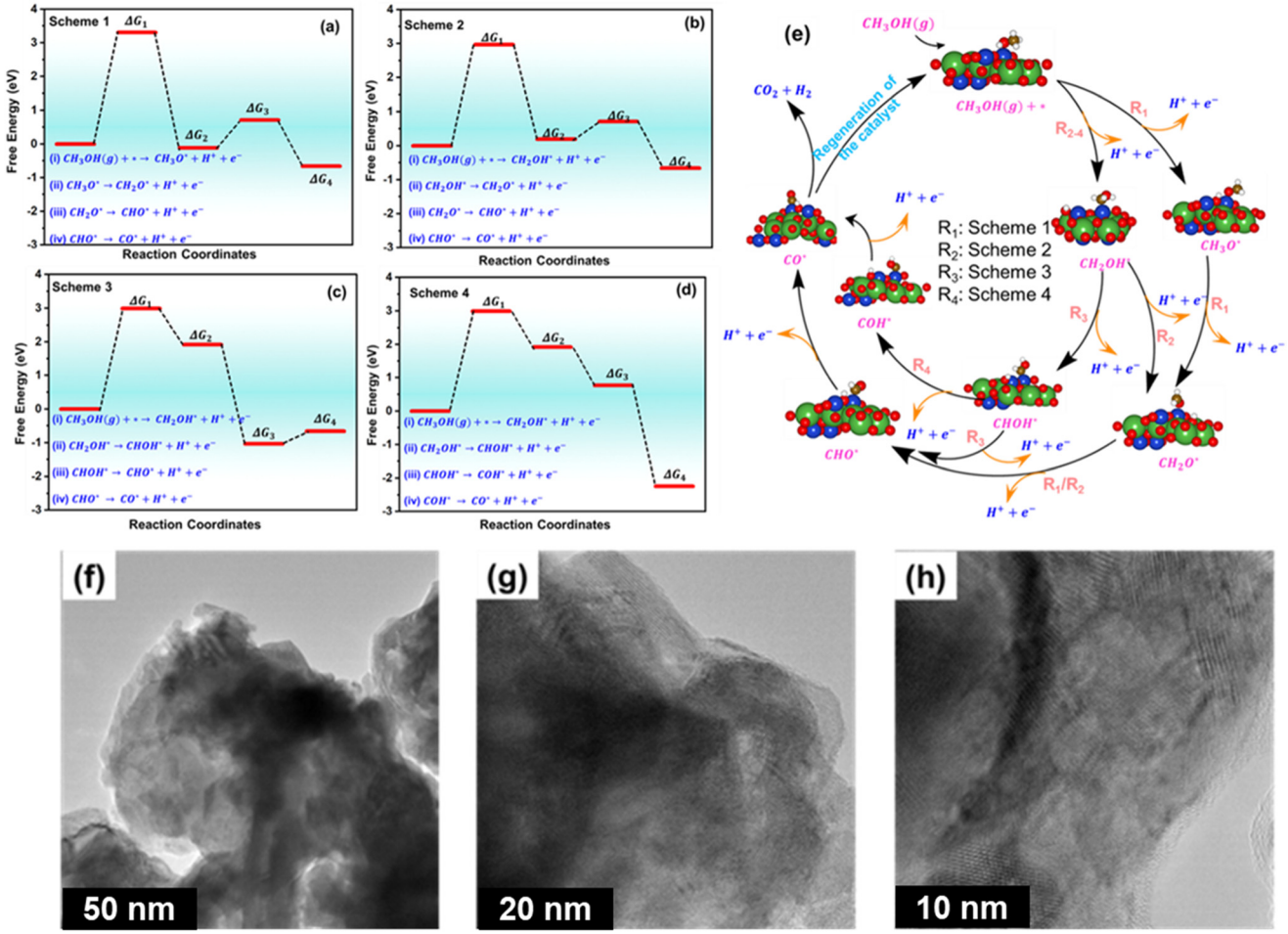

Fig. 6 Schematic representation of the (a)–(e) free energy diagram for the MOR using different mechanistic schemes. The * represents the active surface of the LCO catalyst. (f)–(h) HRTEM image of the LCO catalyst at different resolutions. Color code: red: oxygen, green: lanthanum, grey: nickel, blue: copper, black: zinc, white: hydrogen, and brown: carbon.

result in the lowest charge-transfer resistance and highest electronic conductivity among the catalysts. However, elucidating the methanol oxidation mechanism on the LCO surface through experimental analysis remains challenging. Thus, to unravel the reaction mechanism occurring on the surface of the LCO catalyst, DFT calculations were conducted. The detailed mechanism of methanol oxidation over the LCO catalyst is depicted in Fig. 6.

Reaction mechanism

Based on the experimental analysis, LCO has been identified as a promising catalyst for the MOR. This section explores how different intermediates are adsorbed during the electrochemical oxidation of methanol.[78,85] To elucidate the complete MOR mechanism, various potential elementary reactions were evaluated. Methanol dehydrogenation into CO* and H* on the LCO surface is considered to proceed through four distinct pathways. These pathways are systematically summarized in eqn (1)–(4) as follows:

$$CH_3OH^* \rightarrow CH_3O^* + H^* \rightarrow CH_2O^* + H^* \rightarrow CHO^* + H^* \rightarrow CO^* + H^* \text{ (Scheme 1)} \quad (1)$$

$$CH_3OH^* \rightarrow CH_2OH^* + H^* \rightarrow CH_2O^* + H^* \rightarrow CHO^* + H^* \rightarrow CO^* + H^* \text{ (Scheme 2)} \quad (2)$$

$$CH_3OH^* \rightarrow CH_2OH^* + H^* \rightarrow CHOH^* + H^* \rightarrow CHO^* + H^* \rightarrow CO^* + H^* \text{ (Scheme 3)} \quad (3)$$

$$CH_3OH^* \rightarrow CH_2OH^* + H^* \rightarrow CHOH^* + H^* \rightarrow COH^* + H^* \rightarrow CO^* + H^* \text{ (Scheme 4)} \quad (4)$$

These pathways are mainly categorized into two types: (i) initial activation of the O–H bond (Scheme 1) and (ii) initial activation of the C–H bond (Schemes 2–4). Further investigation examines the different intermediates generated from the dissociation of CH_3OH, as illustrated in Fig. 6 and the SI (section S12 and Fig. S14a).

Scheme 1 outlines a pathway where oxidation begins with the dissociation of the O–H bond in methanol, followed by the removal of one, two, and three hydrogen

atoms from the methyl group to yield CO. Scheme 2 starts with the removal of the first hydrogen atom from the methyl group of methanol (CH_3OH), followed by the sequential removal of hydrogen atoms from the hydroxyl group and the second and third hydrogen atoms from the methyl group. Scheme 3 describes the removal of two hydrogen atoms (the first and second) from the methyl group of CH_3OH, followed by the sequential removal of a hydrogen atom from the hydroxyl group and the third hydrogen atom from the C-atom. Finally, Scheme 4 involves the sequential removal of all three hydrogen atoms from the C-atom, followed by the removal of a hydrogen atom from the hydroxyl group of CH_3OH. A detailed discussion of these reaction pathways is provided in the SI (section S12 and Fig. S14).

Fig. 6 illustrates the adsorbed intermediates on the LCO surface. The analysis reveals that the Cu site is the most favourable for CH_3OH adsorption due to the availability of the Cu-d orbital at the Fermi level, which facilitates CH_3OH oxidation. Consequently, the theoretical analysis focuses on the Cu site for the MOR. Fig. 6f–h presents the HRTEM topography of LCO at different resolutions.

The methanol oxidation can proceed *via* the dissociation of either the C–H or O–H bond, differentiating the pathway outlined in Scheme 1 from those in Schemes 2–4, as mentioned above. Preliminary experimental and theoretical results suggest that the LCO catalyst is particularly effective for the MOR *via* Scheme 3, which involves C–H bond dissociation. In contrast, Schemes 1 and 2 exhibit weaker binding of intermediates, leading to their exclusion from optimal pathways. Both Schemes 3 and 4 demonstrate a strong interaction of LCO with intermediates, making them feasible due to their favourable energy profiles. However, Scheme 4 shows strong CO adsorption, resulting in a more negative Gibbs free energy and subsequent CO poisoning. Conversely, Scheme 3 exhibits weaker CO binding (Gibbs free energy of −0.66 eV), allowing CO to desorb from the LCO catalyst surface with minimal energy input. Therefore, Scheme 3 emerges as the most efficient pathway among the feasible routes.

To gain a deeper understanding of the influence of various adsorption intermediates on the LCO catalyst, crystal orbital Hamilton population (COHP) analyses were conducted as shown in the SI (section S12 and Fig. S14b). The spin-polarized COHP plots for α- and β-spin electrons in all adsorbed intermediates on the LCO catalyst are presented in the SI (section S12 and Fig. S14b). The COHP analysis reveals that bonding contributions are represented by negative values (right), while anti-bonding contributions are indicated by positive values (left). Compared to CH_3O adsorbed on the LCO catalyst, CH_2OH demonstrates a reduced anti-bonding orbital population, leading to an increase in the binding strength of this intermediate. Similarly, the CHO intermediate exhibits a decrease in anti-bonding orbital population compared to the COH intermediate. Integral COHP (ICOHP) values further corroborate the adsorption behaviour of intermediates on the LCO catalyst surface. The ICOHP values for all types of intermediates adsorbed on LCO are provided in the SI (section S12 and Table S2). Orbital interactions, particularly between 3d(Cu)–2p(C) and 3d(Cu)–2p(O), play a crucial role in the MOR. The ICOHP values indicate that the 3d(Cu)–2p(C) bonding interaction in the CHOH adsorbed intermediate (−2.40 eV) is stronger than the 3d(Cu)–2p(O) interaction (−1.33 eV), which further validates the C–H activation being more preferable than C–O activation.

To gain deeper insight into the reaction mechanism and role of the Cu atom in electrooxidation at each stage of the reaction, DOS and differential charge density analyses ($\rho(C_{\text{LCO-intermediate}}) - \rho_{(\text{intermediate})} - \rho_{(C_{\text{LCO}})}$) were performed (see SI section S14 and Fig. S14c and d). Results show that the Cu 3d orbital at the Fermi level reduces the number of anti-bonding states below the Fermi level, highlighting the strong adsorption capability of LCO for adsorbate molecules. The electron density at the Fermi level across all intermediates suggests efficient electron transfer and robust adsorption of intermediates on the LCO catalyst. Details on the orbital interactions between LCO and the intermediates are provided in SI section S12. Charge density difference plots for the most plausible reaction pathway (Scheme 3) show a significant increase in localized charge density at the LCO–intermediate interface, indicating strong interactions. This redistribution of charge reveals that metallic Cu covalently interacts with the active site of the intermediates. Electrons accumulate at the intermediates' active site and are depleted around the Cu atom of the LCO catalyst, as shown in the cyan and yellow areas in SI section S12 and Fig. S14d. These results are consistent with experimental findings and contribute to the improved electrical conductivity, as confirmed by the DOS calculations.

The comparison of MOR performances on the LCO catalyst with and without oxygen defects is also considered in the present investigation. The detailed analysis is provided in SI section S13 and Fig. S15. The calculated relative Gibbs free energies are provided in SI section S13 and Table S3. Calculated results clearly indicate that Scheme 3 is thermodynamically preferred for the MOR activity on the LCO surface without oxygen defects, compared to its defective counterpart. However, intrinsic oxygen vacancies in Ln-based metal oxides are known to enhance oxygen mobility and improve the kinetics of catalysis.[86,87] Despite this, the weaker adsorption of CHO species on the oxygen-deficient LCO surface further limits its catalytic efficiency. Therefore, based on the energy profiles and adsorption properties, Scheme 3, which represents the LCO surface without oxygen defects, emerges as the most efficient pathway among the feasible routes. Further, the comparative analysis of the LCO catalyst with other reported catalysts for the MOR are provided in SI section S14 and Table S4.

Conclusions

This study explores the electrocatalytic performance of lanthanum-based metal oxide catalysts, LNO, LCO, and LZO for methanol oxidation reactions (MORs), forecasting the LCO as the most promising catalyst for clean energy production. The catalysts were synthesized using a sustainable sol–gel method and characterized by PXRD, FESEM, and XPS, which confirmed their successful formation with well-defined crystalline phases and uniform microstructures. Electrochemical analysis revealed that LCO exhibited superior MOR activity compared to LNO and LZO, with a notable peak at 1.27 V *versus* RHE. These results highlight LCO's unique electronic properties, supported by DFT calculations, which indicated that the preferred methanol oxidation mechanism on LCO involves the C–H bond dissociation pathway. A key innovation of this study is the identification of LCO's exceptional anti-CO poisoning behavior. CO stripping analysis, along with ^{13}C NMR, ^{1}H-NMR, and FTIR spectroscopy, demonstrated that CO efficiently desorbs from the LCO surface, preventing CO accumulation and mitigating poisoning effects. This behavior is crucial for maintaining the stability and activity of the catalyst during the reaction. LCO's strong interaction with intermediates and favorable energy profiles make it particularly efficient in the MOR, while also preventing CO poisoning, a major limitation in many electrocatalytic systems. The findings underscore the potential of LCO as a high-performance, sustainable catalyst for methanol oxidation, with significant implications for renewable energy applications. This work contributes valuable insights into the optimization of lanthanum-based catalysts, highlighting LCO's potential in fuel cells and other electrochemical devices.

Conflicts of interest

The authors declare no competing financial interest.

Data availability

Supplementary information: Materials and methods, energy and *k*-point convergence test, EDS analysis, XRD and XPS analysis, FTIR spectrum of LMO, electrooxidation of methanol, band structure analysis of LMO, electron localization function (ELF), elementary steps in the MOR reaction involving electron transfer, along with their corresponding reaction free energy expressions, CO-stripping curve, ^{13}C NMR, ^{1}H-NMR, FTIR analysis after electrolysis, comparison of MOR performances on the LCO catalyst with and without oxygen defects, and comparison of MOR performances with other catalysts. See DOI: **https://doi.org/10.1039/D5CY00827A**.

All the data supporting the findings of this article are provided in the SI.

Acknowledgements

We are thankful to funding agency DST-SERB (EEQ/2023/000424, ECR/2018/002346 and EEQ/2019/000656) Delhi, India, for providing the financial support. We are also thankful to the Director, National Institute of Technology Warangal for providing the facilities. One of the authors Pooja is also thankful to the Ministry of Education (MoE), formerly the Ministry of Human Resource Development (MHRD) for providing a Senior Research Fellowship (SRF). We would also like to thank IIT Roorkee for providing the XPS facility, CeNS Bangalore for the HRTEM facility, and NIT Warangal for the FESEM and XRD facilities. We acknowledge the National Supercomputing Mission (NSM) for providing computing resources of 'PARAM Himalaya' at IIT Mandi, which is implemented by C-DAC and supported by the Ministry of Electronics and Information Technology (MeitY) and Department of Science and Technology (DST), Government of India.

References

1 S. S. Munjewar and S. B. Thombre, Effect of current collector roughness on performance of passive direct methanol fuel cell, *Renewable Energy*, 2019, **138**, 272–283.
2 A. Hamnett, Mechanism and electrocatalysis in the direct methanol fuel cell, *Catal. Today*, 1997, **38**, 445–457.
3 L. Yaqoob, T. Noor and N. Iqbal, Recent progress in development of efficient electrocatalyst for methanol oxidation reaction in direct methanol fuel cell, *Int. J. Energy Res.*, 2021, **45**, 6550–6583.
4 J. Wang, B. Zhang, W. Guo, L. Wang, J. Chen, H. Pan and W. Sun, Toward Electrocatalytic Methanol Oxidation Reaction: Longstanding Debates and Emerging Catalysts, *Adv. Mater.*, 2023, **35**, 2211099.
5 H. Tian, Y. Yu, Q. Wang, J. Li, P. Rao, R. Li, Y. Du, C. Jia, J. Luo, P. Deng, Y. Shen and X. Tian, Recent advances in two-dimensional Pt based electrocatalysts for methanol oxidation reaction, *Int. J. Hydrogen Energy*, 2021, **46**, 31202–31215.
6 R. Yu, Y. Zhang, S. Deng, R. Zhu, S. Zhang, J. Zhang, Y. Zhao and Z. Xia, Platinum Alloys for Methanol Oxidation Electrocatalysis: Reaction Mechanism and Rational Design of Catalysts with Exceptional Activity and Stability, *Catalysts*, 2024, **14**, 60.
7 G. Xu, R. Si, J. Liu, L. Zhang, X. Gong, R. Gao, B. Liu and J. Zhang, Directed self-assembly pathways of three-dimensional Pt/Pd nanocrystal superlattice electrocatalysts for enhanced methanol oxidation reaction, *J. Mater. Chem. A*, 2018, **6**, 12759–12767.
8 F. Saleem, B. Ni, Y. Yong, L. Gu and X. Wang, Ultra-small Tetrametallic Pt-Pd-Rh-Ag Nanoframes with Tunable Behavior for Direct Formic Acid/Methanol Oxidation, *Small*, 2016, **12**, 5261–5268.
9 J. Xie, Q. Zhang, L. Gu, S. Xu, P. Wang, J. Liu, Y. Ding, Y. F. Yao, C. Nan, M. Zhao, Y. You and Z. Zou, Ruthenium–

platinum core–shell nanocatalysts with substantially enhanced activity and durability towards methanol oxidation, *Nano Energy*, 2016, **21**, 247–257.

10 X. Wang, L. Chen and B. Li, A density functional theory study of methanol dehydrogenation on the PtPd3(111) surface, *Int. J. Hydrogen Energy*, 2015, **40**, 9656–9669.

11 X. Peng, D. Chen, X. Yang, D. Wang, M. Li, C.-C. Tseng, R. Panneerselvam, X. Wang, W. Hu, J. Tian and Y. Zhao, Microwave-Assisted Synthesis of Highly Dispersed PtCu Nanoparticles on Three-Dimensional Nitrogen-Doped Graphene Networks with Remarkably Enhanced Methanol Electrooxidation, *ACS Appl. Mater. Interfaces*, 2016, **8**, 33673–33680.

12 Y. Lou, C. Li, X. Gao, T. Bai, C. Chen, H. Huang, C. Liang, Z. Shi and S. Feng, Porous Pt Nanotubes with High Methanol Oxidation Electrocatalytic Activity Based on Original Bamboo-Shaped Te Nanotubes, *ACS Appl. Mater. Interfaces*, 2016, **8**, 16147–16153.

13 T. Yang, Q. Xue, X. Yu, X. Qi, R. Wu, S. Lu, Z. Gu, J. Jiang and Y. Nie, DFT Study on Methanol Oxidation Reaction Catalyzed by PtmPdn Alloys, *Coatings*, 2022, **12**, 918.

14 H. Li, Y. Pan, D. Zhang, Y. Han, Z. Wang, Y. Qin, S. Lin, X. Wu, H. Zhao, J. Lai, B. Huang and L. Wang, Surface oxygen-mediated ultrathin PtRuM (Ni, Fe, and Co) nanowires boosting methanol oxidation reaction, *J. Mater. Chem. A*, 2020, **8**, 2323–2330.

15 Y.-W. Zhou, Y.-F. Chen, K. Jiang, Z. Liu, Z.-J. Mao, W.-Y. Zhang, W.-F. Lin and W.-B. Cai, Probing the enhanced methanol electrooxidation mechanism on platinum-metal oxide catalyst, *Appl. Catal., B*, 2021, **280**, 119393.

16 J. Rossmeisl, P. Ferrin, G. A. Tritsaris, A. U. Nilekar, S. Koh, S. E. Bae, S. R. Brankovic, P. Strasser and M. Mavrikakis, Bifunctional anode catalysts for direct methanol fuel cells, *Energy Environ. Sci.*, 2012, **5**, 8335–8342.

17 Y. Zuo, W. Sheng, W. Tao and Z. Li, Direct methanol fuel cells system–A review of dual-role electrocatalysts for oxygen reduction and methanol oxidation, *J. Mater. Sci. Technol.*, 2022, **114**, 29–41.

18 F. Lyu, M. Cao, A. Mahsud and Q. Zhang, Interfacial engineering of noble metals for electrocatalytic methanol and ethanol oxidation, *J. Mater. Chem. A*, 2020, **8**, 15445–15457.

19 J. Parbey, F. Adu-Gyamfi, M. Gyan, J. Parbey, F. Adu-Gyamfi and M. Gyan, Progress in Cathode Materials for Methanol Fuel Cells, in *Methanol Fuel in Transportation Sector and Fuel Cells*, IntechOpen, 2024.

20 Y. Jiang, H. Fu, Z. Liang, Q. Zhang and Y. Du, Rare earth oxide based electrocatalysts: synthesis, properties and applications, *Chem. Soc. Rev.*, 2024, **53**, 714–763.

21 S. S. Nandi, V. Adimule, S. A. Kadapure and S. S. Kerur, Rare Earth Based Nanocomposite Materials for Prominent Performance Supercapacitor: A Review, *Appl. Mech. Mater.*, 2022, **908**, 3–18.

22 X. Shi, B. Cao, J. Liu, J. Zhang and Y. Du, Rare-Earth-Based Metal–Organic Frameworks as Multifunctional Platforms for Catalytic Conversion, *Small*, 2021, **17**, 2005371.

23 M. A. Yatoo, F. Habib, A. H. Malik, M. J. Qazi, S. Ahmad, M. A. Ganayee and Z. Ahmad, Solid-oxide fuel cells: A critical review of materials for cell components, *MRS Commun.*, 2023, **13**, 378–384.

24 M. A. Yatoo, F. Habib, A. H. Malik, M. J. Qazi, S. Ahmad, M. A. Ganayee and Z. Ahmad, *ChemRxiv*, 2023, preprint, DOI: **10.26434/chemrxiv-2023-txrf8**.

25 S. C. McGuire, C. Koenigsmann, C. C. Chou, X. Tong and S. S. Wong, Lanthanum-based double perovskite nanoscale motifs as support media for the methanol oxidation reaction, *Catal. Sci. Technol.*, 2022, **12**, 613–629.

26 S. Dou, X. Wang and S. Wang, Rational Design of Transition Metal-Based Materials for Highly Efficient Electrocatalysis, *Small Methods*, 2019, **3**, 1800211.

27 L. Li, S. Tan, K. L. Salvatore and S. S. Wong, Nanoscale Perovskites as Catalysts and Supports for Direct Methanol Fuel Cells, *Chem. – Eur. J.*, 2019, **25**, 7779–7797.

28 H. Yi, S. Liu, C. Lai, G. Zeng, M. Li, X. Liu, B. Li, X. Huo, L. Qin, L. Li, M. Zhang, Y. Fu, Z. An and L. Chen, Recent Advance of Transition-Metal-Based Layered Double Hydroxide Nanosheets: Synthesis, Properties, Modification, and Electrocatalytic Applications, *Adv. Energy Mater.*, 2021, **11**, 2002863.

29 Pooja and R. Pawar, Understanding Methanol Electro-Oxidation Pathways on Nd-Based Metal Oxides via DFT and Electrochemical Studies, *Langmuir*, 2025, **41**, 16203–16215.

30 M. Alaydrus, M. Sakaue and H. Kasai, A DFT+U study on the contribution of 4f electrons to oxygen vacancy formation and migration in Ln-doped CeO2, *Phys. Chem. Chem. Phys.*, 2016, **18**, 12938–12946.

31 A. Majid, M. Azmat, U. A. Rana, S. U.-D. Khan and E. Alzahrani, A computational study of magnetic exchange interactions of 3d and 4f electrons in Ti-Ce co-doped AlN, *Mater. Chem. Phys.*, 2016, **179**, 316–321.

32 W. Gao, Z. Xia, F. Cao, J. C. Ho, Z. Jiang and Y. Qu, Comprehensive Understanding of the Spatial Configurations of CeO2 in NiO for the Electrocatalytic Oxygen Evolution Reaction: Embedded or Surface-Loaded, *Adv. Funct. Mater.*, 2018, **28**, 1706056.

33 Y. Cheng, H. Nan, Q. Li, Y. Luo and K. Chu, A Rare-Earth Samarium Oxide Catalyst for Electrocatalytic Nitrogen Reduction to Ammonia, *ACS Sustainable Chem. Eng.*, 2020, **8**, 13908–13914.

34 X. Ding, X. Kong, X. Wang, J. Jiang and C. Cui, Characterization and optimization of Ln1.7Sr0.3CuO4 (Ln = La, Nd)-based cathodes for intermediate temperature solid oxide fuel cells, *J. Alloys Compd.*, 2010, **502**, 472–476.

35 T. L. Meyer, R. Jacobs, D. Lee, L. Jiang, J. W. Freeland, C. Sohn, T. Egami, D. Morgan and H. N. Lee, Strain control of oxygen kinetics in the Ruddlesden-Popper oxide La1.85Sr0.15CuO4, *Nat. Commun.*, 2018, **9**, 92.

36 M. Al Daroukh, V. V. Vashook, H. Ullmann, F. Tietz and I. Arual Raj, Oxides of the AMO3 and A2MO4-type: structural stability, electrical conductivity and thermal expansion, *Solid State Ionics*, 2003, **158**, 141–150.
37 X. Chen, Y. Tan, Z. Li, T. Liu, Y. Song, S. Zhai, N. Yu, Z. Shao and M. Ni, Advanced Air Electrodes for Reversible Protonic Ceramic Electrochemical Cells: A Comprehensive Review, *Adv. Mater.*, 2025, 2418620.
38 S. Yanagisawa, A. Takeda, K. Inagaki, I. Hamada and Y. Morikawa, Search for a Self-Regenerating Perovskite Catalyst with Ab Initio Thermodynamics II: Cu-Doped Layered Perovskites with K2NiF4 Structure, *Catal. Lett.*, 2014, **144**, 736–743.
39 J.-C. Grenier, A. Wattiaux, N. Lagueyte, J. C. Park, E. Marquestaut, J. Etourneau and M. Pouchard, A new superconductor obtained by electrochemical oxidation of La2CuO4, *Phys. C*, 1991, **173**, 139–144.
40 Y. Li, J. Huang, L. Cao, J. Wu and J. Fei, Optical properties of La2CuO4 and La2 − xCaxCuO4 crystallites in UV–vis–NIR region synthesized by sol–gel process, *Mater. Charact.*, 2012, **64**, 36–42.
41 E. Boehm, J.-M. Bassat, P. Dordor, F. Mauvy, J.-C. Grenier and Ph. Stevens, Oxygen diffusion and transport properties in non-stoichiometric Ln2 − xNiO4 + δ oxides, *Solid State Ionics*, 2005, **176**, 2717–2725.
42 P. Chandrasekharan Meenu, P. K. Samanta, T. Yoshida, N. J. English, S. P. Datta, S. A. Singh, S. Dinda, C. Chakraborty and S. Roy, Electro-Oxidation Reaction of Methanol over La2–xSrxNiO4+δ Ruddlesden–Popper Oxides, *ACS Appl. Energy Mater.*, 2022, **5**, 503–515.
43 J. Li, L. Li, J. Wang, A. Cabot and Y. Zhu, Boosting Hydrogen Evolution by Methanol Oxidation Reaction on Ni-Based Electrocatalysts: From Fundamental Electrochemistry to Perspectives, *ACS Energy Lett.*, 2024, **9**, 853–879.
44 R. B. Araujo, D. Martín-Yerga, E. C. dos Santos, A. Cornell and L. G. M. Pettersson, Elucidating the role of Ni to enhance the methanol oxidation reaction on Pd electrocatalysts, *Electrochim. Acta*, 2020, **360**, 136954.
45 A. Hussain, N. Jabeen, S. Zafar, M. F. A. Taleb and M. M. Ibrahim, Theoretical investigation of Ruddlesden Popper phase La2XO4(X = Zn, Ca, Mg, and Be) compounds with multifunctional properties for flexible photovoltaic applications, *J. Electroceram.*, 2025, DOI: **10.1007/s10832-025-00395-z**.
46 A. Sajid, E. Pervaiz, H. Ali, T. Noor and M. M. Baig, A perspective on development of fuel cell materials: Electrodes and electrolyte, *Int. J. Energy Res.*, 2022, **46**, 6953–6988.
47 Z. Yavari, M. Noroozifar and M. Khorasani-Motlagh, Multifunctional catalysts toward methanol oxidation in direct methanol fuel cell, *J. Appl. Electrochem.*, 2015, **45**, 439–451.
48 X. Zhou, B. Hu, Z. Chen, F. Delgado and R. Srivastava, Nonprecious Metal Perovskite Electrocatalysts for Direct Methanol Fuel Cells, *Electrochem. Solid-State Lett.*, 2005, **8**, A616.
49 B. Levasseur and S. Kaliaguine, Effect of the rare earth in the perovskite-type mixed oxides AMnO3 (A=Y, La, Pr, Sm, Dy) as catalysts in methanol oxidation, *J. Solid State Chem.*, 2008, **181**, 2953–2963.
50 M. E. Scofield, C. Koenigsmann, D. Bobb-Semple, J. Tao, X. Tong, L. Wang, C. S. Lewis, M. B. Vukmirovic, Y. Zhu, R. R. Adzic and S. S. Wong, Correlating the chemical composition and size of various metal oxide substrates with the catalytic activity and stability of as-deposited Pt nanoparticles for the methanol oxidation reaction, *Catal. Sci. Technol.*, 2016, **6**, 2435–2450.
51 K. Zhu, F. Shi, X. Zhu and W. Yang, The roles of oxygen vacancies in electrocatalytic oxygen evolution reaction, *Nano Energy*, 2020, **73**, 104761.
52 B. H. Toby and R. B. Von Dreele, GSAS-II: the genesis of a modern open-source all purpose crystallography software package, *J. Appl. Crystallogr.*, 2013, **46**, 544–549.
53 I. Shaheen, S. Ata, H. Aslam, W. Mnif, M. Iqbal, T. Ali, A. Nazir, A. Ali and A. Manikandan, Carbon nitride effect on La2NiO4 and La2CuO4 structural, morphological and photocatalytic properties, *J. Mol. Struct.*, 2025, **1321**, 139979.
54 X. Zhou, Y. Chen, C. Li, L. Zhang, X. Zhang, X. Ning, L. Zhan and J. Luo, Construction of LaNiO3 nanoparticles modified g-C3N4 nanosheets for enhancing visible light photocatalytic activity towards tetracycline degradation, *Sep. Purif. Technol.*, 2019, **211**, 179–188.
55 P. Chandrasekharan Meenu, P. K. Samanta, T. Yoshida, N. J. English, S. P. Datta, S. A. Singh, S. Dinda, C. Chakraborty and S. Roy, Electro-Oxidation Reaction of Methanol over La2–xSrxNiO4+δ Ruddlesden–Popper Oxides, *ACS Appl. Energy Mater.*, 2022, **5**, 503–515.
56 R. P. Forslund, W. G. Hardin, X. Rong, A. M. Abakumov, D. Filimonov, C. T. Alexander, J. T. Mefford, H. Iyer, A. M. Kolpak, K. P. Johnston and K. J. Stevenson, Exceptional electrocatalytic oxygen evolution via tunable charge transfer interactions in La0.5Sr1.5Ni1−xFexO4±δ Ruddlesden-Popper oxides, *Nat. Commun.*, 2018, **9**, 3150.
57 A. Aguadero, J. A. Alonso, M. J. Martínez-Lope, M. T. Fernández-Díaz, M. J. Escudero and L. Daza, In situ high temperature neutron powder diffraction study of oxygen-rich La2NiO4+δ in air: correlation with the electrical behaviour, *J. Mater. Chem.*, 2006, **16**, 3402–3408.
58 T. Inprasit, P. Limthongkul and S. Wongkasemjit, Sol–Gel and Solid-State Synthesis and Property Study of La2 − xSrxNiO4 (x ≤ 0.8), *J. Electrochem. Soc.*, 2010, **157**, B1726.
59 M. Sukumar and L. J. Kennedy, Catalytic Conversion of Methanol to Formaldehyde Over La2CuO4 Nanoparticles, *J. Nanosci. Nanotechnol.*, 2019, **19**, 826–832.
60 M. Sukumar, L. J. Kennedy, J. J. Vijaya, B. Al-Najar and M. Bououdina, Co2+ substituted La2CuO4/LaCoO3 perovskite nanocomposites: synthesis, properties and heterogeneous catalytic performance, *New J. Chem.*, 2018, **42**, 18128–18142.
61 S. S. Maluf and E. M. Assaf, La2−xCexCu1−yZnyO4 perovskites for high temperature water-gas shift reaction, *J. Nat. Gas Chem.*, 2009, **18**, 131–138.

62 M. Sukumar, L. J. Kennedy, J. J. Vijaya, B. Al-Najar, M. Bououdina and G. Mudhana, Structural, optical, and magnetic properties of Ca2+ doped La2CuO4 perovskite nanoparticles, *Vacuum*, 2019, **167**, 407–415.

63 M. Sukumar, M. Agila, A. Sutha, V. Ravi, A. M. Al-Enizi, M. Ubaidullah, M. S. Samdani, M. Sundararajan and B. Pandit, Temperature-dependent phase transition: structural, optical, magnetic and dielectric properties of La2CuO4 perovskite nanoparticles, *J. Mater. Sci.: Mater. Electron.*, 2022, **33**, 26144–26156.

64 M. M. Rahman, W. A. Adeosun and A. M. Asiri, Fabrication of selective and sensitive chemical sensor development based on flower-flake La2ZnO4 nanocomposite for effective non-enzymatic sensing of hydrogen peroxide by electrochemical method, *Microchem. J.*, 2020, **159**, 105536.

65 I. Ahmad, M. A. Jamal, M. Iftikhar, A. Ahmad, S. Hussain, H. Asghar, M. Saeed, A. B. Yousaf, R. R. Karri, N. S. Al-kadhi, M. Ouladsmane, A. Ghfar and S. Khan, Lanthanum-Zinc Binary Oxide Nanocomposite with Promising Heterogeneous Catalysis Performance for the Active Conversion of 4-Nitrophenol into 4-Aminophenol, *Coatings*, 2021, **11**, 537.

66 A. Manikandan, E. Manikandan, B. Meenatchi, S. Vadivel, S. K. Jaganathan, R. Ladchumananandasivam, M. Henini, M. Maaza and J. S. Aanand, Rare earth element (REE) lanthanum doped zinc oxide (La: ZnO) nanomaterials: Synthesis structural optical and antibacterial studies, *J. Alloys Compd.*, 2017, **723**, 1155–1161.

67 N. Sulaiman, Y. Yulizar and D. O. B. Apriandanu, Eco-friendly method for synthesis of La2O3 nanoparticles using Physalis angulata leaf extract, *AIP Conf. Proc.*, 2018, **2023**, 020105.

68 I. Shaheen, S. Ata, H. Aslam, W. Mnif, M. Iqbal, T. Ali, A. Nazir, A. Ali and A. Manikandan, Carbon nitride effect on La2NiO4 and La2CuO4 structural, morphological and photocatalytic properties, *J. Mol. Struct.*, 2025, **1321**, 139979.

69 M. K. Skakov, S. K. Kabdrakhmanova, K. Akatan, A. M. Zhilkashinova, E. Shaimardan, M. M. Beisebekov, K. Nurgamit, V. V. Baklanov, Y. T. Koyanbayev, A. Z. Miniyazov, I. A. Sokolov and N. M. Mukhamedova, La2CuO4 Electrode Material for Low Temperature Solid Oxide Fuel Cells, *ES Mater. Manuf.*, 2023, **22**, 969.

70 A. Rahmani and J. Saffari, Preparation, Structure and Selected Catalytic Properties of La2CuO4 Nano Mixed Metal Oxides, *J. Nanostruct.*, 2016, **6**, 301–306.

71 P. Odier, M. Leblanc and J. Choisnet, Structural characterization of an orthorhombic form of La2NiO4, *Mater. Res. Bull.*, 1986, **21**, 787–796.

72 M. L. Fontaine, C. Laberty-Robert, M. Verelst, J. Pielaszeck, P. Lenormand, F. Ansart and P. Tailhades, Synthesis of La2NiO4+δ oxides by sol–gel process: Structural and microstructural evolution from amorphous to nanocrystallized powders, *Mater. Res. Bull.*, 2006, **41**, 1747–1753.

73 I. Ahmad, M. A. Jamal, M. Iftikhar, A. Ahmad, S. Hussain, H. Asghar, M. Saeed, A. B. Yousaf, R. R. Karri, N. S. Al-kadhi, M. Ouladsmane, A. Ghfar and S. Khan, Lanthanum-Zinc Binary Oxide Nanocomposite with Promising Heterogeneous Catalysis Performance for the Active Conversion of 4-Nitrophenol into 4-Aminophenol, *Coatings*, 2021, **11**, 537.

74 G. Kresse and J. Furthmüller, Efficiency of ab-initio total energy calculations for metals and semiconductors using a plane-wave basis set, *Comput. Mater. Sci.*, 1996, **6**, 15–50.

75 G. Kresse and J. Furthmüller, Efficient iterative schemes for ab initio total-energy calculations using a plane-wave basis set, *Phys. Rev. B: Condens. Matter Mater. Phys.*, 1996, **54**, 11169–11186.

76 P. E. Blöchl, Projector augmented-wave method, *Phys. Rev. B: Condens. Matter Mater. Phys.*, 1994, **50**, 17953–17979.

77 H. J. Monkhorst and J. D. Pack, Special points for Brillouin-zone integrations, *Phys. Rev. B: Solid State*, 1976, **13**, 5188–5192.

78 X. Wang, S. Xi, W. S. V. Lee, P. Huang, P. Cui, L. Zhao, W. Hao, X. Zhao, Z. Wang, H. Wu, H. Wang, C. Diao, A. Borgna, Y. Du, Z. G. Yu, S. Pennycook and J. Xue, Materializing efficient methanol oxidation via electron delocalization in nickel hydroxide nanoribbon, *Nat. Commun.*, 2020, **11**, 4647.

79 S. Zhou, X. Miao, X. Zhao, C. Ma, Y. Qiu, Z. Hu, J. Zhao, L. Shi and J. Zeng, Engineering electrocatalytic activity in nanosized perovskite cobaltite through surface spin-state transition, *Nat. Commun.*, 2016, **7**, 11510.

80 A. Grimaud, O. Diaz-Morales, B. Han, W. T. Hong, Y.-L. Lee, L. Giordano, K. A. Stoerzinger, M. T. M. Koper and Y. Shao-Horn, Activating lattice oxygen redox reactions in metal oxides to catalyse oxygen evolution, *Nat. Chem.*, 2017, **9**, 457–465.

81 J. T. Mefford, W. G. Hardin, S. Dai, K. P. Johnston and K. J. Stevenson, Anion charge storage through oxygen intercalation in LaMnO3 perovskite pseudocapacitor electrodes, *Nat. Mater.*, 2014, **13**, 726–732.

82 R. P. Forslund, C. T. Alexander, A. M. Abakumov, K. P. Johnston and K. J. Stevenson, Enhanced Electrocatalytic Activities by Substitutional Tuning of Nickel-Based Ruddlesden–Popper Catalysts for the Oxidation of Urea and Small Alcohols, *ACS Catal.*, 2019, **9**, 2664–2673.

83 X. Lin, Y.-C. Huang, Z. Hu, L. Li, J. Zhou, Q. Zhao, H. Huang, J. Sun, C.-W. Pao, Y.-C. Chang, H.-J. Lin, C.-T. Chen, C.-L. Dong, J.-Q. Wang and L. Zhang, 5f Covalency Synergistically Boosting Oxygen Evolution of UCoO4 Catalyst, *J. Am. Chem. Soc.*, 2022, **144**, 416–423.

84 B. Zhang, X. Zheng, O. Voznyy, R. Comin, M. Bajdich, M. García-Melchor, L. Han, J. Xu, M. Liu, L. Zheng, F. P. García de Arquer, C. T. Dinh, F. Fan, M. Yuan, E. Yassitepe, N. Chen, T. Regier, P. Liu, Y. Li, P. De Luna, A. Janmohamed, H. L. Xin, H. Yang, A. Vojvodic and E. H. Sargent,

Homogeneously dispersed multimetal oxygen-evolving catalysts, *Science*, 2016, **352**, 333–337.

85 J. K. Nørskov, J. Rossmeisl, A. Logadottir, L. Lindqvist, J. R. Kitchin, T. Bligaard and H. Jónsson, Origin of the Overpotential for Oxygen Reduction at a Fuel-Cell Cathode, *J. Phys. Chem. B*, 2004, **108**, 17886–17892.

86 S.-Y. Tsai and K.-Z. Fung, Progress and Prospects of Intermediate-Temperature Solid Oxide Fuel Cells, in *Energy Storage and Conversion Materials*, CRC Press, 2023.

87 J. Xia, S. Chen, Z. Guo, C. Chen, J. Zhang, Z. Zhang and L. Jia, Low-Carbon Fabrication of Fluorine-Free Superhydrophobic Copper-Based Materials for Acquiring Freshwater, *Langmuir*, 2025, **41**, 16591–16609.

